

A 1-bit electronically reconfigurable beam steerable metasurface reflectarray with multiple polarization manipulations

Yan Shi(史琰), Xi-Ya Xu(徐茜雅), Shao-Ze Wang(王少泽), Wen-Yue Wei(魏文岳), and Quan-Wei Wu(武全伟)
Citation: Chin. Phys. B, 2024, 33 (**1**): 014201. DOI: 10.1088/1674-1056/acfa8a
Journal homepage: http://cpb.iphy.ac.cn; http://iopscience.iop.org/cpb

What follows is a list of articles you may be interested in

Creation mechanism of electron-positron pair on equally spaced multiple localized fields

Chuan-Ke Li(李传可), Nan-Sheng Lin(林南省), Xian-Xian Zhou(周鲜鲜),Miao Jiang(江淼), and Ying-Jun Li(李英骏)
Chin. Phys. B, 2023, 32 (**9**): 094202. DOI: 10.1088/1674-1056/acd7cd

High efficiency and high transmission asymmetric polarization converter with chiral metasurface in visible and near-infrared region

Yuhang Gao(高雨航), Yu Tian(田宇), Qingguo Du(杜庆国), Yuanli Wang(王原丽), Qin Fu(付琴), Qiang Bian(卞强), Zhengying Li(李政颖), Shuai Feng(冯帅), and Fangfang Ren(任芳芳)
Chin. Phys. B, 2023, 32 (**7**): 074201. DOI: 10.1088/1674-1056/acb9eb

Evolution of polarization singularities accompanied by avoided crossing in plasmonic system

Yi-Xiao Peng(彭一啸), Qian-Ju Song(宋前举), Peng Hu(胡鹏), Da-Jian Cui(崔大健), Hong Xiang(向红), and De-Zhuan Han(韩德专)
Chin. Phys. B, 2023, 32 (**1**): 014201. DOI: 10.1088/1674-1056/ac728d

Beam steering characteristics in high-power quantum-cascade lasers emitting at ~4.6 μm

Yong-Qiang Sun(孙永强), Jin-Chuan Zhang(张锦川), Feng-Min Cheng(程凤敏), Chao Ning(宁超), Ning Zhuo(卓宁), Shen-Qiang Zhai(翟慎强), Feng-Qi Liu(刘峰奇), Jun-Qi Liu(刘俊岐), Shu-Man Liu(刘舒曼), and Zhan-Guo Wang(王占国)
Chin. Phys. B, 2021, 30 (**3**): 034211. DOI: 10.1088/1674-1056/abd6fe

Polarization manipulation of bright-dark vector bisolitons

Yan Zhou(周延), Xiaoyan Lin(林晓艳), Meisong Liao(廖梅松), Guoying Zhao(赵国营), and Yongzheng Fang(房永征)
Chin. Phys. B, 2021, 30 (**3**): 034208. DOI: 10.1088/1674-1056/abd76d

---

A 1-bit electronically reconfigurable beam steerable metasurface reflectarray with multiple polarization manipulations

Yan Shi(史琰)[†], Xi-Ya Xu(徐茜雅), Shao-Ze Wang(王少泽), Wen-Yue Wei(魏文岳), and Quan-Wei Wu(武全伟)

School of Electronic Engineering, Xidian University, Xi'an 710071, *China*

(Received 24 July 2023; revised manuscript received 9 September 2023; accepted manuscript online 18 September 2023)

A 1-bit electronically controlled metasurface reflectarray is presented to achieve beam steering with multiple polarization manipulations. A metsurface unit cell loaded by two PIN diodes is designed. By switching the two PIN diodes between ON and OFF states, the isotropic and anisotropic reflections can be flexibly achieved. For either the isotropic reflection or the anisotropic reflection, the two operation states achieve the reflection coefficients with approximately equal magnitude and 180° out of phase, thus giving rise to the isotropic/anisotropic 1-bit metasurface unit cells. With the 1-bit unit cells, a 12-by-12 metasurface reflectarray is optimally designed and fabricated. Under either *y*- or *x*-polarized incident wave illumination, the reflectarray can achieve the co-polarized and cross-polarized beam scanning, respectively, with the peak gains of 20.08 dBi and 17.26 dBi within the scan range of about ±50°. With the right-handed circular polarization (RHCP) excitation, the left-handed circular polarization (LHCP) radiation with the peak gain of 16.98 dBic can be achieved within the scan range of ±50°. Good agreement between the experimental results and the simulation results are observed for 2D beam steering and polarization manipulation capabilities.

Keywords: electronically controlled, metasurface reflectarray, beam steering, polarization manipulation

PACS: 42.25.Bs, 42.81.Gs, 81.05.Xj **DOI:** 10.1088/1674-1056/acfa8a

1. Introduction

With rapid development of wireless communication technology, high-performance antennas and arrays become essential to ensure good communication quality in a dynamic and complicate environment. The high-gain beam steerable radiation characteristic is highly demanded to reduce multipath fading and environment interference. As an alternative to high-cost phased array antenna, reconfigurable reflectarray antenna (RRA) can achieve adaptive pattern scanning by reconfigurable metasurface surface and thus has attracted much interest in recent years.[1,2] Owing to low cost, easy fabrication and light weight, the RRA becomes a promising solution in the field of 5G/6G wireless communication, satellite communication, etc. In real-life complicated environment, polarization mismatch significantly degrades the quality and reliability of wireless communication links. Thus, the merging of the polarization diversity technology into the RRA design is an effective method to enhance the anti-interference ability and improve the transmission efficiency of the wireless communication.[3]

In order to generate beam agility of the RRA, the phase shift required by the RRA is manipulated. Compared with mechanical control, e.g., micromotors or actuators,[4,5] it is more convenient and rapid to adjust the phase shift by using tunable materials such as liquid crystal[6] and graphene[7] or active components including varactor diodes,[8,9] PIN diode,[10,11] and micro-electro-mechanical systems (MEMS).[12,13] In the conventional RRA design, it is desirable to realize a reflection phase range of 2π for perfect phase compensation. By means of continuously tunable materials or components, the reflection phase between 0° and 360° can be obtained. However, the RRA design based on the continuous phase shift is technically complicated. Instead, a discrete phase shift scheme by quantizing 2π phase range into a group of discrete phase state can greatly simplify the RRA design.[14–23] In Ref. [19], a dual-band 1-bit 16×16 RRA composed of a rectangular patch with two PIN diodes was developed. In terms of the quantization phase of 180°, 1-bit phase shifts for *x*-polarization at 12.5 GHz and for *y*-polarization at 14.25 GHz are generated, thus realizing dual-band co-polarization beam scanning. A 1-bit 16×16 RRA with circular polarization (CP) characteristic has been developed.[20] By switching two PIN diodes in a circularly shaped patch element between forward and reverse bias and meanwhile rotating the patch by 90°, 1-bit CP element is obtained, thus achieving 2-D co-polarized beam steering under the left-handed circular polarization wave illumination. In addition, a 1-bit 16×16 reflectarray was designed for 2D cross-polarized beam scanning.[23] By switching two PIN diodes placed in tetra-arrow element from ON state to OFF state, the 1-bit phase shift for the cross-polarization reflection can be obtained under the linear polarization wave illumination. To date, existing works on designing the RRA are limited to single polarization characteristic, i.e., sole linear or circular co-polarization and sole linear cross-polarization. No reports on RRA designs with multiple polarization characteristics have been found.

[†]Corresponding author. E-mail: shiyan@mail.xidian.edu.cn

© 2024 Chinese Physical Society and IOP Publishing Ltd

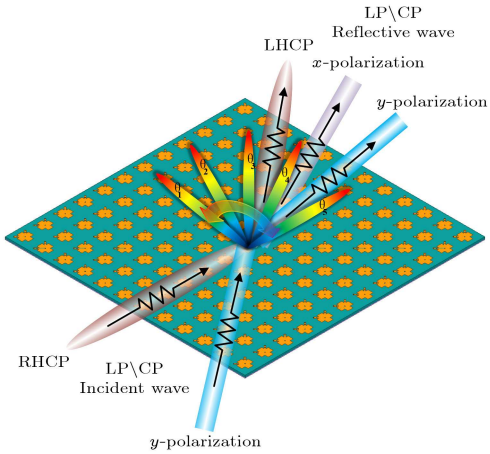


Fig. 1. Beam scanning RRA with multiple polarization characteristics.

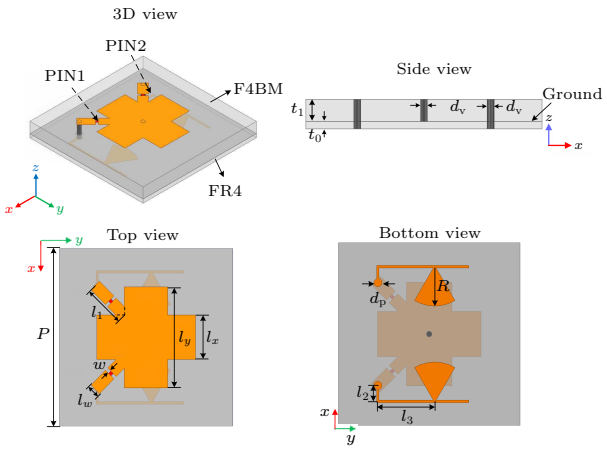


Fig. 2. Anisotropic metasurface RRA unit cell. Dimensions of the unit cell (unit: mm): $P = 16$, $l_x = 4$, $l_1 = 3.55$, $d_p = 0.7$, $l_3 = 5$, $t_0 = 1.5$, $l_y = 9.1$, $l_w = 1.1$, $R = 3.55$, $t_1 = 0.5$, $w = 0.3$, $d_v = 0.5$, and $l_2 = 1.5$.

In this paper, we present an electronically reconfigurable 12×12 metasurface reflectarray with beam steering and polarization manipulating capabilities, as shown in Fig. 1. The proposed metasurface unit cell is composed of a cross patch with two stubs connected to two PIN diodes. By independently adjusting the biasing voltage of each PIN diode, the metasurface unit cell exhibits the isotropic and anisotropic reflection characteristics. Thus two sets of 1-bit phase shifts corresponding to the co-polarization radiation and the cross-polarization radiation, respectively, can be obtained. With a linearly polarized feeding horn excitation, 2D co-polarization and cross-polarization beam steering can be achieved by the proposed optimal RRA. When a feeding horn with right-handed circular polarization (RHCP) characteristic is used, the RRA generates the 2D LHCP beam scanning. The simulation and measurement results are given to validate the proposed design.

2. Anisotropic metasurface RRA unit cell design

Figure 2 gives the proposed unit cell of the metasurface RRA. The unit cell is composed of the top substrate F4B with relative permittivity of 2.65 and tangent loss of 0.005 and the bottom substrate with the relative permittivity of 4.4 and tangent loss of 0.026. A metallic ground is placed between two substrates. A cross patch is fabricated on the top surface of the F4B and two stubs along $\varphi = 45°$ and $\varphi = -45°$ directions loaded by two PIN diodes (SMP 1340-040 LF from Skyworks Solution Inc.), respectively, are connected to the cross patch. At the end of each stub, a metallic via is used to connect the stub with the DC biasing circuit. A metallic via placed in the middle of the cross patch is introduced to connect the cross patch with the ground. The DC biasing circuit for the PIN diode is fabricated on the bottom surface of the FR4. In the biasing circuit, a radial stub is designed to choke high-frequency signal. The biasing line is placed at the location where the weakest fields exist.

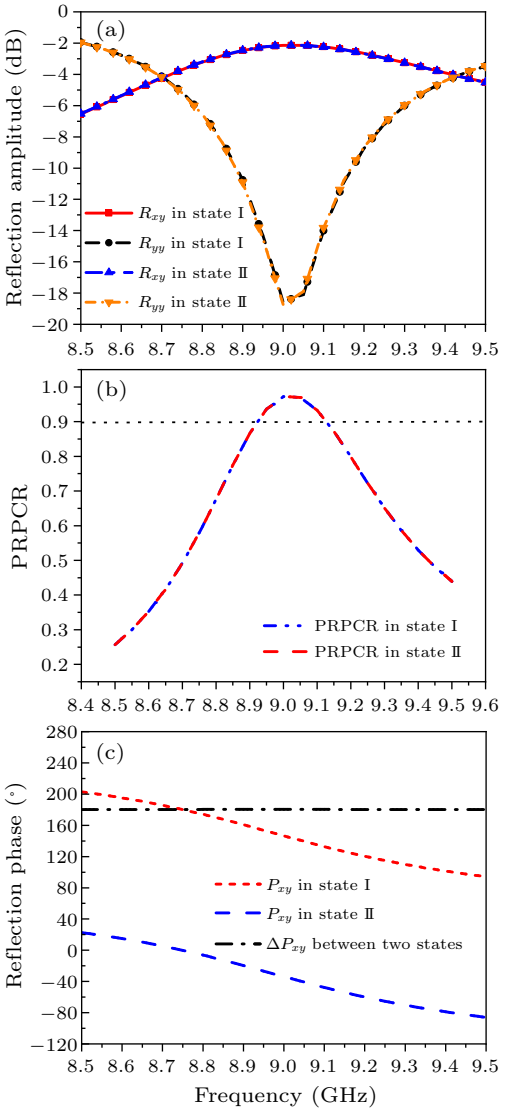


Fig. 3. Performance of the unit cell in states I and II for TE polarized incidence. (a) Reflection magnitude. (b) PRPCR. (c) Reflection phase.

In order to elaborate the anisotropic characteristic of the proposed element, consider a transverse electric (TE) polarized wave, i.e., an incoming wave with y-polarized electric field, normally incident on the unit cell enclosed by the pe-

riodic boundary. When the DC voltage is applied in the biasing circuit, two PIN diodes are switched between OFF and ON states, thus giving rise to four operation states, as shown in Table 1. In the state I, the PIN diode 1 is in ON state and the PIN diode 2 is in OFF state. The resulting co-polarized and cross-polarized components of the reflection coefficient are shown in Fig. 3(a). It can be seen that the cross-polarized component of the reflection coefficient R_{xy} is larger than the co-polarized one R_{yy} in the band 8.7–9.4 GHz. Note that the corresponding equivalent circuits of the PIN diode in ON and OFF states shown in Fig. 4 are used for simulation of the reflection coefficient. On the other hand, when the PIN diode 1 is in the OFF state and the PIN diode 2 in the ON state, which is called state Ⅱ, the obtained reflection coefficient is plotted in Fig. 3(a). The R_{xy} and R_{yy} in the state Ⅱ are almost same as those in the state I, and the R_{xy} is larger than the R_{yy} in the band of 8.7–9.4 GHz. It is worth noticing that the R_{yy} varies sharply with the change of the frequency. This is due to the fact that the imperfect performance of PIN diode results in the rapid change of the equivalent impedance of the proposed element.

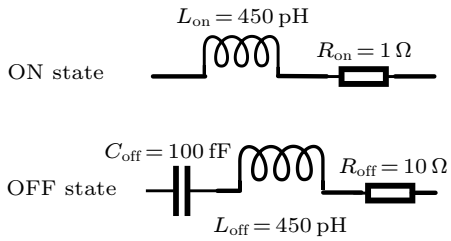


Fig. 4. Equivalent circuits of PIN diode in ON and OFF states.

Table 1. Operations states of the proposed unit cell.

State	PIN 1 & 2	Polarization	Phase difference between two states
I	ON, OFF	Cross-polarized	180°
Ⅱ	OFF, ON		
Ⅲ	ON, ON	Co-polarized	180°
Ⅳ	OFF, OFF		

In order to measure the anisotropic performance, i.e., polarization conversion (PC), the partial reflection polarization conversion rate (PRPCR) is defined as

$$\mathrm{PRPCR} = |R_{xy}|^2/(|R_{xy}|^2 + |R_{yy}|^2 + |T_{xy}|^2 + |T_{yy}|^2), \quad (1)$$

in which T_{xy} and T_{yy} are the cross-polarized and co-polarized components of the transmission coefficient, respectively. Owing to the use of the ground, the transmission coefficients T_{xy} and T_{yy} are zero. It is worth pointing out that the PRPCR, which is different from the conventional polarization conversion rate (PCR), i.e., $|R_{xy}|^2$,[24,25] represents the ratio of the cross-polarized reflection wave to the total reflection wave regardless of the loss effect of the unit cell, and thus can better demonstrate anisotropic characteristic. As shown in Fig. 3(b), the band of the proposed unit cell for PRPCR $\geqslant 0.9$ covers 8.88–9.17 GHz in the two states. In addition, Fig. 3(c) shows the phase of the cross-polarized component of the reflection coefficient in the states I and Ⅱ, i.e., P_{xy}. It can be found that in the band of 8.5–9.5 GHz, the phase difference of the cross-polarized component between the two states ΔP_{xy} is π.

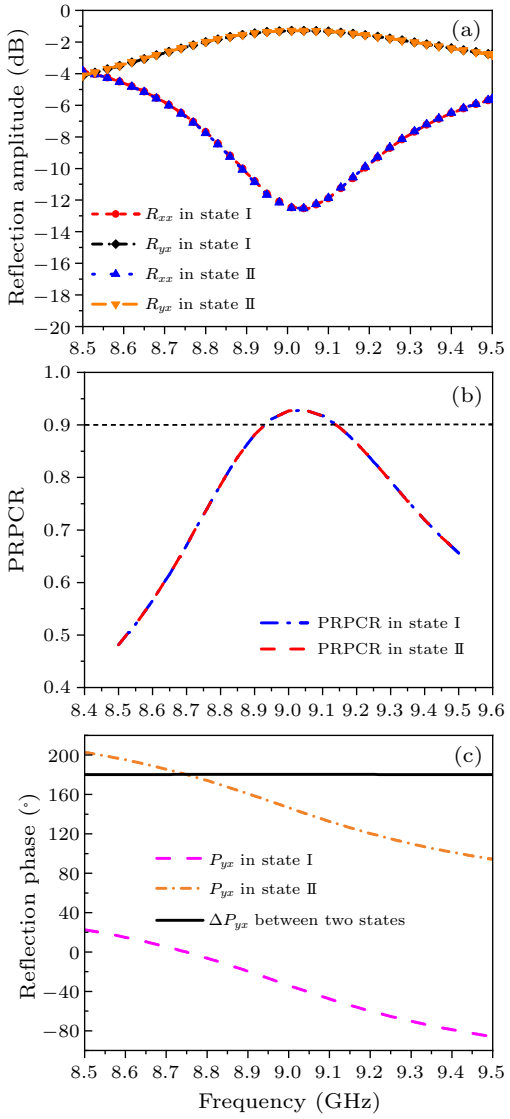


Fig. 5. Performance of the unit cell in states I and Ⅱ for TM polarized incidence. (a) Reflection magnitude. (b) PRPCR. (c) Reflection phase.

Similarly, for transverse magnetic (TM) polarized normal incidence, i.e., an incoming wave with x-polarization electric field, the cross-polarized component of the reflection coefficient R_{yx} is larger than the co-polarized one R_{xx} in the band of 8.5–9.5 GHz in both the states I and Ⅱ, as shown in Fig. 5(a). Moreover, the R_{yx} and the R_{xx} in the state I are equal to those in the state Ⅱ. According to Fig. 5(b), the band of the proposed unit cell for PRPCR $\geqslant 0.9$ covers 8.93–9.14 GHz in the two states. In addition, the phase difference of the cross-polarized component between the two states ΔP_{yx} is π in the band of 8.5–9.5 GHz, as shown in Fig. 5(c).

In the state Ⅲ, both the PIN diodes 1 and 2 are in ON state, and the corresponding reflection coefficient is given in Fig. 6. It can be observed that the R_{yy} in TE polarization and the R_{xx} in TM polarization are approximately equal to 1, and are far larger than the R_{xy} in TE polarization and the R_{yx} in TM polarization in the band of 8.5–9.5 GHz. In the state Ⅳ with both the PIN diodes 1 and 2 in OFF states, the co-polarized and cross-polarized components of the reflection coefficient are approximately equal to those in the state Ⅲ. Moreover, the co-polarized component of the reflection coefficient is far larger than the cross-polarized one in the band of 8.5–9.5 GHz for both TE and TM polarizations. In addition, the phase difference of the co-polarized component between the state Ⅲ and the state Ⅳ for TE and TM polarizations is $180^\circ \pm 30^\circ$ in the band of 8.97–9.2 GHz and 8.76–9.02 GHz, respectively. Note that the phase difference between the state Ⅲ and the state Ⅳ is not exactly 180°. This is due to the different variation trends of the reflective phase P_{yy} in two states, which is mainly caused by the parasitic effect of the PIN diodes. It is worthwhile pointing out that the phase difference of 180° is not a necessary requirement. On the one hand, the 1-bit quantized phase method is indeed an approximation to the accurate phase distribution required by the RRA. On the other hand, the optimization procedure based on the reference phase can be employed to determine the RRA layout for the optimal radiation performance. The details about the 1-bit quantized phase method and the reference phase based optimization are given in the following section.

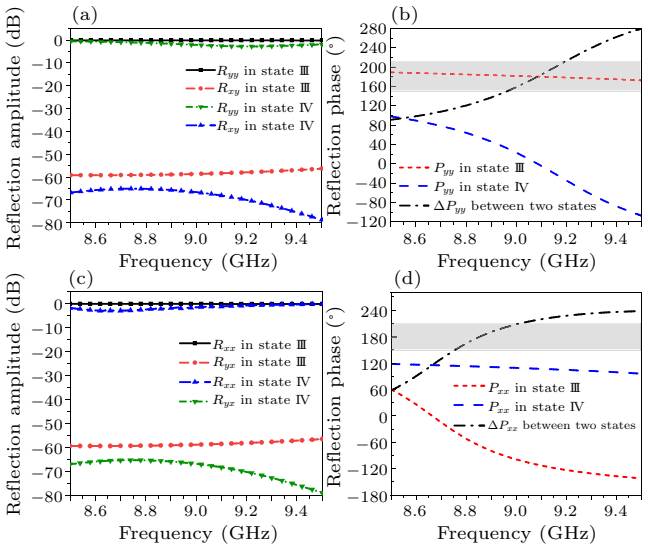


Fig. 6. Reflection magnitudes and phases in states Ⅲ and Ⅳ. (a) Magnitude for TE polarized incidence. (b) Phase for TE polarized incidence. (c) Magnitude for TM polarized incidence. (d) Phase for TM polarized incidence.

In order to further elaborate the anisotropic and isotropic responses of the proposed element in different operation states, the surface current distributions on the element at 8.9 GHz in the four states are plotted in Fig. 7 under *y*-polarized wave incidence. In the state I, the PIN 1 is in the ON state, and thus the microstrip line in the direction of $\varphi = 225^\circ$ is connected to the cross patch. The *y*-polarized incident electric field induces the current flowing along $\varphi = 225^\circ$. On the other hand, with the PIN 2 in the OFF state, the microstrip line in the direction of $\varphi = 135^\circ$ is disconnected to the cross patch, thus resulting in the equivalent capacitance between them. The current flowing along $\varphi = 135^\circ$ is induced by the *y*-polarized incident electric field. Therefore, the induced current flows from the microstrip line in the direction of $\varphi = 225^\circ$ to the microstrip line in the direction of $\varphi = 135^\circ$ via the cross patch. In this scenario, the superposition of surface currents gives rise to the total current flowing along $-x$ axis direction, achieving the PC. In the state Ⅱ, the PIN 1 is in the OFF state and the PIN 2 is in ON state. Similar to the state I, the current flows from the microstrip line in the direction of $\varphi = 135^\circ$ to the microstrip line in the direction of $\varphi = 225^\circ$ via the cross patch. Therefore, the total current obtained by the superposition of surface currents flows along *x* direction, exhibiting the PC characteristic. Since the total current in the state Ⅱ is opposite to that in the state I, the phase difference of the cross-polarized components of the reflection coefficient between the state I and the state Ⅱ is π.

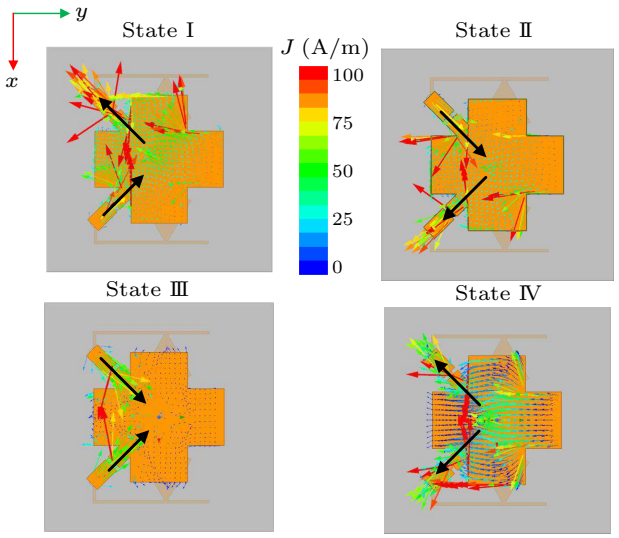


Fig. 7. Surface current distributions on the RRA element at 8.9 GHz in four states.

In the state Ⅲ, both the PIN 1 and the PIN 2 are in the ON state, and thus the microstrip lines in the directions of $\varphi = 225^\circ$ and $\varphi = 135^\circ$ are connected to the cross patch simultaneously. In this scenario, the induced current flows from two microstrip lines to the cross patch, and thus the total current by superposing the surface currents flows along *y* direction. In the state Ⅳ with both the PIN 1 and PIN 2 in OFF state, the microstrip lines in the directions of $\varphi = 225^\circ$ and $\varphi = 135^\circ$ are disconnected to the cross patch simultaneously, and the induced current flows from the cross patch to two microstrip lines owing to the equivalent capacitances between the cross patch and the microstrip lines. The total current obtained by the superposition of surface currents flows along $-y$ direction.

In this scenario, the phase difference of the co-polarized components of the reflection coefficient between the state Ⅲ and the state Ⅳ is π.

3. Metasurface RRA design for beam scanning

According to the above discussions, we can know that the proposed metasurface unit cell is of both anisotropic and isotropic reflection characteristics in different operation states. The reflection phase of 180° can be achieved in either between the state I and the state Ⅱ or between the state Ⅲ and the state Ⅳ. With the unit cell, we can build up a 1-bit isotropic and anisotropic metasurface RRA.

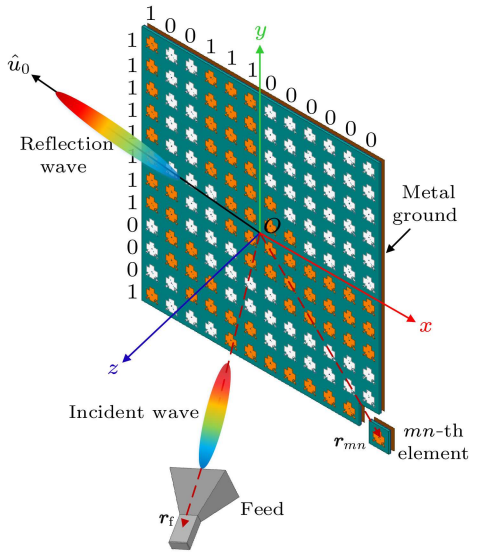


Fig. 8. The RRA diagram.

3.1. Co-polarized and cross-polarized 1-bit RRA

As shown in Fig. 8, consider an RRA composed of $M \times N$ unit cells in xoy plane. The feeding horn with the radiation pattern $F(\boldsymbol{r})$ and the phase center at $\boldsymbol{r}_f$ illuminates the reflectarray. The reradiated field from the reflectarray along $\hat{u}$ direction can be calculated by[11]

$$\boldsymbol{E}(\hat{u}) = \sum_{m=1}^{M}\sum_{n=1}^{N} F(\boldsymbol{r}_{mn}\cdot\boldsymbol{r}_f)A(\boldsymbol{r}_{mn}\cdot\hat{u}_0)A(\hat{u}\cdot\hat{u}_0) \times \exp\{-\mathrm{j}k_0[|\boldsymbol{r}_{mn}-\boldsymbol{r}_f|+\boldsymbol{r}_{mn}\cdot\hat{u}]+\mathrm{j}\Delta\phi_{mn}\}, \quad (2)$$

in which $\boldsymbol{r}_{mn}$ is the location of the mnth unit cell, i.e., the unit cell in mth row and nth column of the reflectarray, $A(\boldsymbol{r})$ is the element pattern, and $\hat{u}_0$ is the direction of the desirable beam. The required compensation phase of the mnth unit cell is obtained as

$$\Delta\phi_{mn} = k_0(\boldsymbol{r}_{mn}\cdot\hat{u}_0 + |\boldsymbol{r}_{mn}-\boldsymbol{r}_f|). \quad (3)$$

Note that all unit cells are considered to have the same pattern and the coupling between them is neglected in Eq. (2).

According to the phase distribution of the reflectarray solved by Eq. (2), the phase behavior can be digitally quantized as

$$\phi_{mn}^{q} = \begin{cases} 0°, & 0° \leqslant \mathrm{PV}(\Delta\phi_{mn}+\phi_{\mathrm{ref}}) < 180°, \\ 180°, & 180° \leqslant \mathrm{PV}(\Delta\phi_{mn}+\phi_{\mathrm{ref}}) < 360°, \end{cases} \quad (4)$$

where $\mathrm{PV}(\phi)$ represents a principle value operation transforming the phase ϕ into the interval [0, 360°], and ϕ_{ref} denotes the reference phase. It can be seen that the introduction of the ϕ_{ref} in Eq. (3) has no effect on magnitude of the electric field solved by Eq. (2). Based on the quantized phase distribution given by Eq. (4), the proposed 1-bit unit cells can be arranged into a reflectarray.

In order to realize the co-polarized radiation, the unit cells operating in the states Ⅲ and Ⅳ are designed as the unit cell 0 and unit cell 1, respectively, with the reflection phases of 0° and 180°. By changing the ϕ_{ref}, the reflectarray layout is adjusted, and thus the optimal radiation performance of the RRA can be achieved.[26] Figure 9 gives the compensation phase distributions with $M = N = 12$ and their digitally quantized layouts without and with the ϕ_{ref} for three radiation beam directions ($\theta = 0°$, $\varphi = 0°$), ($\theta = 50°$, $\varphi = 0°$), and ($\theta = 40°$, $\varphi = 90°$). It can be seen that the quantized layouts have the similar distributions to the compensation phase. Compared to the quantized layout without the ϕ_{ref}, the quantized layouts are slightly adjusted by using the ϕ_{ref}.

For the cross-polarized radiation, the unit cells operating in states I and Ⅱ are designed as the unit cell 0 with the reflection phase of 0° and the unit cell 1 with the reflection phase of 180°, respectively. Similarly, the optimal quantized layouts are solved from Eq. (4) by changing the ϕ_{ref} for different radiation beam directions. Figure 10 shows the required compensation phase distributions and the quantized layouts without and with the ϕ_{ref} for three radiation beam directions ($\theta = 0°$, $\varphi = 0°$), ($\theta = 50°$, $\varphi = 0°$), and ($\theta = 50°$, $\varphi = 90°$). Similar distributions can be observed from the quantized layouts and the compensation phase distributions.

3.2. Circularly polarized 1-bit RRA

In order to achieve the CP radiation, consider an RHCP wave generated by a feeding horn illuminates the reflectarray. Without loss of generality, an incident wave along $-z$ axis is assumed. In this scenario, the incident electric field can be expressed as

$$\boldsymbol{E}_{inc} = |E_i|\,\mathrm{e}^{\mathrm{j}\varphi_i}(\hat{x}+\hat{y}\,\mathrm{e}^{\mathrm{j}\pi/2}), \quad (5)$$

in which $|E_i|\,\mathrm{e}^{\mathrm{j}\varphi_i}$ is the x-component of the incident electric field. When the unit cell operates in the state I, the reflective electric field can be obtained as follows:

$$\boldsymbol{E}_{\mathrm{ref}}^{\mathrm{I}} = |E_i|\,\mathrm{e}^{\mathrm{j}\varphi_i}(\hat{y}|R_{yx}^{\mathrm{I}}|\,\mathrm{e}^{\mathrm{j}\varphi_{yx}^{\mathrm{I}}}+\hat{x}|R_{xy}^{\mathrm{I}}|\,\mathrm{e}^{\mathrm{j}\varphi_{xy}^{\mathrm{I}}}\,\mathrm{e}^{\mathrm{j}\pi/2}), \quad (6)$$

where the cross-polarized components of the reflection coefficients for the TM and TE waves are $|R^{\mathrm{I}}_{yx}|\mathrm{e}^{\mathrm{j}\varphi^{\mathrm{I}}_{yx}}$ and $|R^{\mathrm{I}}_{xy}|\mathrm{e}^{\mathrm{j}\varphi^{\mathrm{I}}_{xy}}$, respectively. According to Figs. 3 and 5, we can know that $|R^{\mathrm{I}}_{yx}| \approx |R^{\mathrm{I}}_{xy}|$ and $\varphi^{\mathrm{I}}_{xy} \approx \varphi^{\mathrm{I}}_{yx} + \pi$. Thus, Eq. (6) can be rewritten as

$$\boldsymbol{E}^{\mathrm{I}}_{\mathrm{ref}} = |E_i||R^{\mathrm{I}}_{yx}|\,\mathrm{e}^{\mathrm{j}\varphi_i}\,\mathrm{e}^{\mathrm{j}\varphi^{\mathrm{I}}_{yx}}(\hat{y} + \hat{x}\mathrm{e}^{\mathrm{j}3\pi/2}). \tag{7}$$

With Eq. (7), the reflective wave along $+z$ direction in the state I is LHCP wave.

On the other hand, for the unit cell operating in the state Ⅱ, the reflective electric field can be obtained as

$$\begin{aligned}\boldsymbol{E}^{\mathrm{II}}_{\mathrm{ref}} &= |E_i||R^{\mathrm{II}}_{yx}|\,\mathrm{e}^{\mathrm{j}\varphi_i}\,\mathrm{e}^{\mathrm{j}\varphi^{\mathrm{II}}_{yx}}(\hat{y} + \hat{x}\mathrm{e}^{-\mathrm{j}\pi/2}) \\ &= |E_i||R^{\mathrm{I}}_{yx}|\,\mathrm{e}^{\mathrm{j}\varphi_i}\,\mathrm{e}^{\mathrm{j}(\varphi^{\mathrm{I}}_{yx}-\pi)}(\hat{y} + \hat{x}\mathrm{e}^{-\mathrm{j}\pi/2}).\end{aligned} \tag{8}$$

Note that in deriving Eq. (8), the conditions of $|R^{\mathrm{II}}_{yx}| \approx |R^{\mathrm{II}}_{xy}| \approx |R^{\mathrm{I}}_{yx}|$, $\varphi^{\mathrm{II}}_{xy} \approx \varphi^{\mathrm{II}}_{yx} - \pi$, and $\varphi^{\mathrm{II}}_{yx} \approx \varphi^{\mathrm{I}}_{yx} - \pi$ have been used. Therefore, the reflective wave in the state Ⅱ is also the LHCP wave. The phase difference of the reflective electric fields between the state I and the state Ⅱ is π. Thus, the unit cells in the states I and Ⅱ are designed as the unit cell 0 and the unit cell 1, respectively. The reflectarray with the LHCP radiation characteristic can be achieved by arranging the unit cells 0 and 1. It is worthwhile noticing that the quantized layout for the CP radiation is same as that for the cross-polarized radiation owing to the use of the unit cells in the states I and Ⅱ. In addition, the RHCP wave can be radiated by the proposed reflectarray if the horn antenna with LHCP characteristic excites the reflectarray.

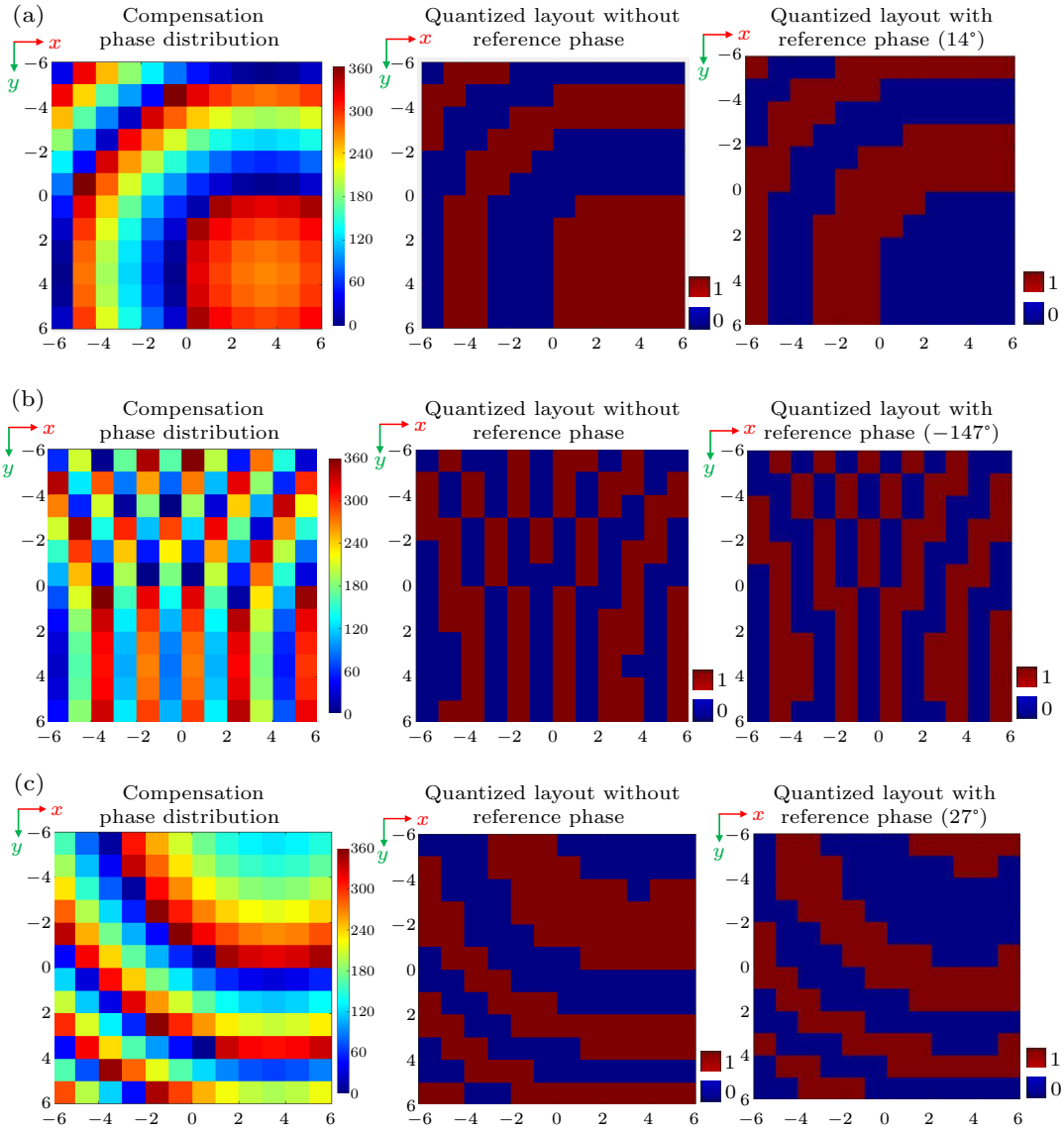


Fig. 9. Phase distributions and the digitally quantized layouts without and with the reference phase for co-polarized beam steering: (a) (0°, 0°) beam, (b) (50°, 0°) beam, (c) (40°, 90°) beam.

It is worthwhile pointing out that with the unit cells in the states Ⅲ and Ⅳ, the reflectarray cannot radiate good RHCP wave for the RHCP wave illumination. This is due to the fact that in the either state Ⅲ or state Ⅳ, the phase difference of the co-polarized components of the reflection coefficients between the TM polarization and the TE polarization is not approximately π, as shown in Figs. 6(b) and (d). Thus the CP radiation performance becomes deteriorated. The main reason is

attributed to effect of the PIN diode on performance of the unit cell. It can be noticed that in the state Ⅲ with two PIN diodes in ON state or the state Ⅳ with two PIN diodes in OFF state, the whole structure is only symmetry about *y* axis. The responses of the corresponding structures for *y*-polarized incidence are distinctly different from those for *x*-polarized incidence. By contrast, the behavior of the unit cell in the state I is similar to that in the state Ⅱ except 180° out-of-phase reflection.

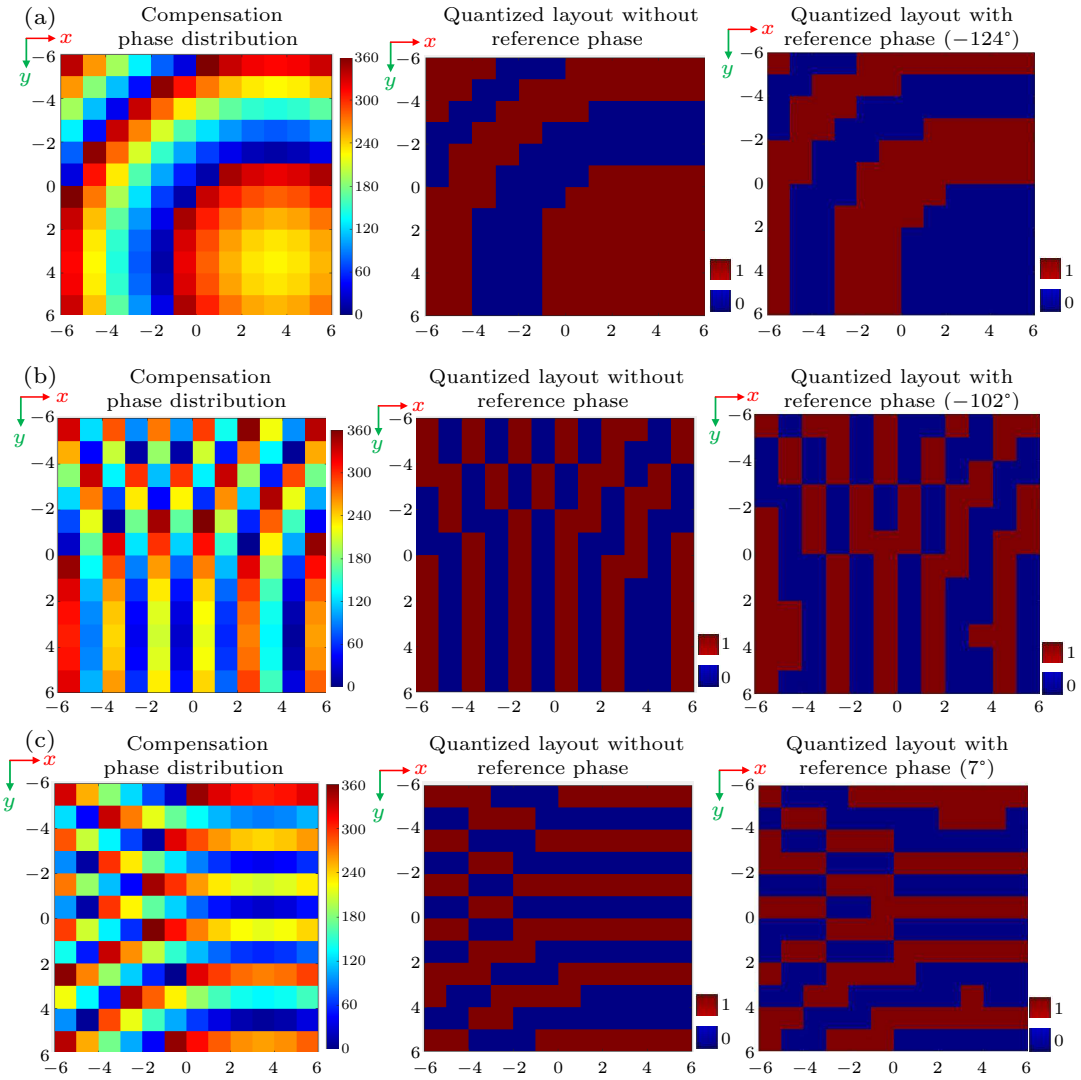


Fig. 10. Phase distributions and the digitally quantized layouts without and with the reference phase for cross-polarized beam scanning: (a) (0°, 0°) beam, (b) (50°, 0°) beam, (c) (50°, 90°) beam.

3.3. Beam scanning performance

A commercial feeding horn (HD-100SGAN15N from Hengda Microwave Inc.) with the operation frequency of 8.2–12.4 GHz is used to excite the reflectarray. The horn with the phase center at (−56.6 mm, −56.5 mm, 226 mm) is placed in a distance of 240 mm from the reflectarray. The focal diameter ratio (F/D) is chosen as 1.25 to ensure good spillover efficiency and illumination efficiency.[27]

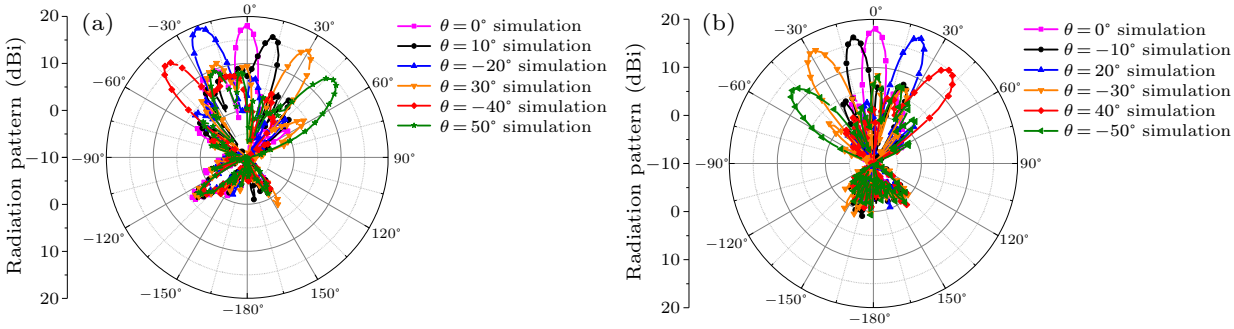


Fig. 11. Co-polarization beam steering performance at 8.9 GHz: (a) *xoz* plane, (b) *yoz* plane.

Figure 11 shows the co-polarization beam steering performance at 8.9 GHz. It can be seen from Fig. 11(a) that in *xoz* plane, the peak gain of 19.42 dBi occurs at the radiation beam along $\theta = -20°$ direction, with aperture efficiency of 21.43% and sidelobe level (SLL) of -12.4 dB. The gain drops from 19.42 dBi to 14.68 dBi when the radiation beam scans from 0° to 50°. The scanning range for the gain difference $\leqslant 3$ dB covers $-40°$ to 40°, with half power beamwidth (HPBW) less than 10° and SLL better than -8.23 dB. In *yoz* plane, the scanning range for the gain drop $\leqslant 3$ dB is from $-40°$ to 40°, where the peak gain of 17.96 dBi and the aperture efficiency of 15.31% and the SLL better than -8.21 dB are obtained according to Fig. 11(b). Furthermore, the radiation pattern in *xoz* plane at 8.9 GHz for the radiation beam along broadside direction is shown in Fig. 12. The co-polarized component is 23 dB larger than the cross-polarized one, ensuring good polarization isolation.

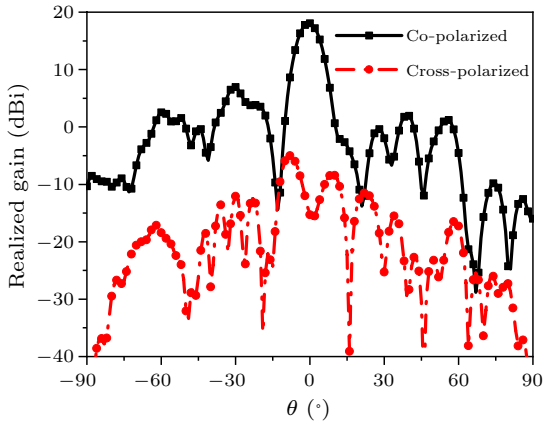


Fig. 12. Pattern at 8.9 GHz for the co-polarized beam along $\theta = 0°$ direction.

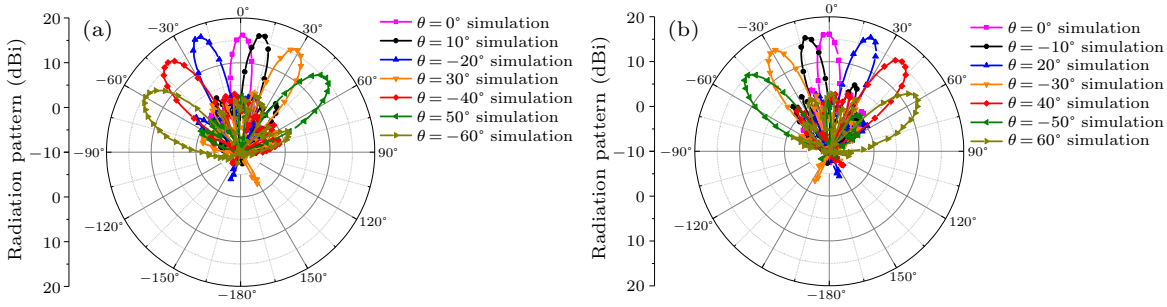


Fig. 13. Cross-polarization beam steering performance at 8.9 GHz: (a) *xoz* plane, (b) *yoz* plane.

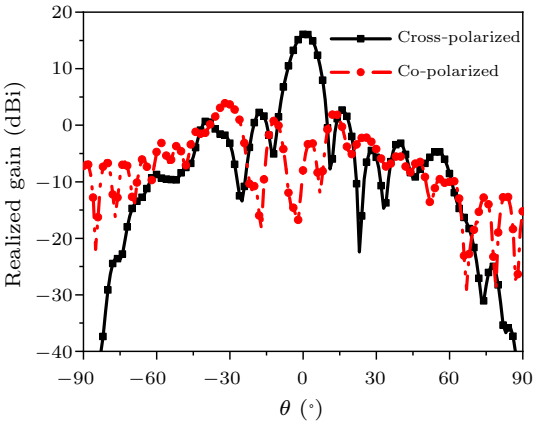


Fig. 14. Pattern at 8.9 GHz for the cross-polarized beam along $\theta = 0°$ direction.

Figure 13 shows the cross-polarized beam scanning performance at 8.9 GHz. In *xoz* plane, the scanning range for gain difference $\leqslant 3$ dB is $\pm 60°$, with the peak gain of 17.41 dBi and the aperture efficiency of 13.49% at the radiation beam along $\theta = -20°$ direction. For different beam directions, the SLL is below -11.8 dB and the HPBW is less than 19°. In *yoz* plane, the scanning range for gain drop $\leqslant 3$ dB is $\pm 50°$. For the radiation beam along $\theta = 20°$ direction, the peak gain is 17.02 dBi with the aperture efficient of 12.33%. When the radiation beam is in the direction of $\theta = 60°$, the gain decreases by 4.15 dB. In the beam scanning range, the SLL better than -10 dB and the HPBW less than 14° are obtained. Note that the peak gains in *xoz* and *yoz* planes for the cross-polarized radiation are less than those of the co-polarized radiation. The main reason is due to the loss of the substrate and the PIN diodes. In addition, it can be seen from Fig. 14 that the co-polarized component is 20 dB less than the cross-polarized one.

Figure 15 gives the LHCP beam scanning performance at 9 GHz under the RHCP wave illumination. It can be observed that when the radiation beam steers from 0° to 50°, the gain drop is 2.52 dBic in *xoz* plane and 2.86 dBic in *yoz* plane. The peak gain of 16.98 dBic and the aperture efficiency of 12.22% in *xoz* plane and the peak gain of 16.96 dBic and the aperture efficiency of 12.16% in *yoz* plane, respectively, are obtained. The SLL better than -10 dB and the HPBW less than $-15°$ are achieved in the beam scanning range. In addition, the LHCP gain is 10 dB larger than the RHCP one, as shown in Fig. 16.

4. Fabrication and measurement of metasurface RRA

The prototype of the proposed metasurface RRA is fabricated, as shown in Fig. 17(a). The whole structure consisting

of a reflectarray, a feeding horn, two control circuit boards. Figure 17(b) shows the 12×12 reflectarray. There are 24 sockets that are placed at the two edges of the bottom surface of the reflectarray, as shown in Fig. 17(c). Each socket can provide 12 independent DC channels for 6 elements. There are 24 flat cables used to connect two control boards and 24 sockets. In each control board, 144 light-emitting diodes (LED) are used to indicate the operation states of the PIN didoes. The LED is lightened when the corresponding PIN diode is in ON state, as shown in Fig. 17(d). The control program corresponding to each digitally quantized layout is written into a 32-bit microcontroller unit (MCU) in the control board, thus realizing the beam steering with multiple polarization manipulations. Due to our measurement limitations, the used feeding horn only radiates a *y*-polarized electric field.

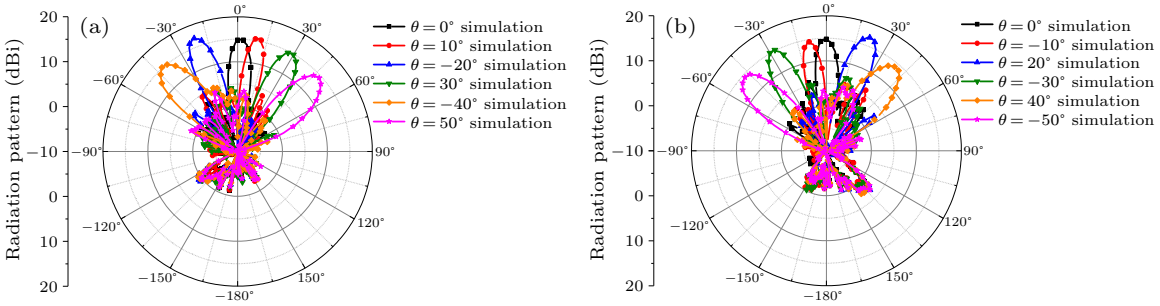


Fig. 15. LHCP beam steering performance at 9 GHz: (a) *xoz* plane, (b) *yoz* plane.

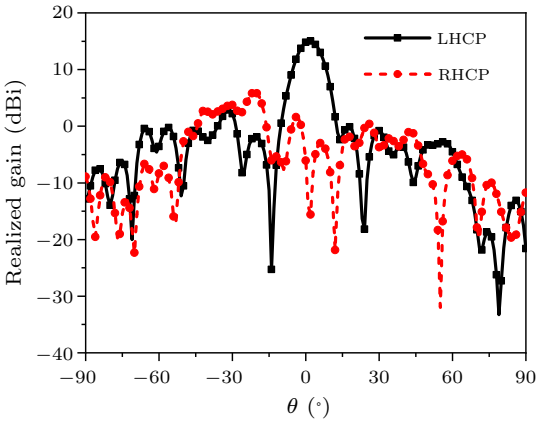


Fig. 16. Pattern at 9 GHz for the CP radiation beam along $\theta = 0°$ direction.

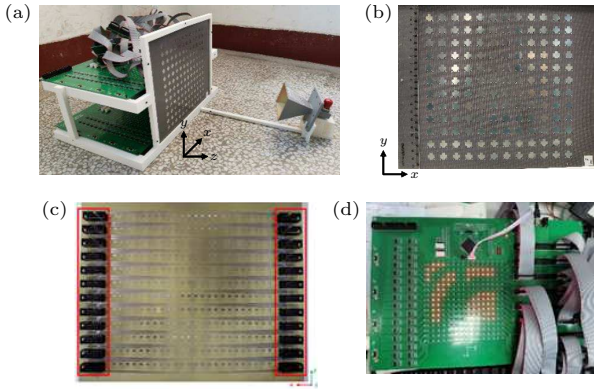


Fig. 17. The fabricated RRA: (a) whole structure, (b) top view of reflectarray, (c) bottom view of reflectarray, (d) control board with LED indicators.

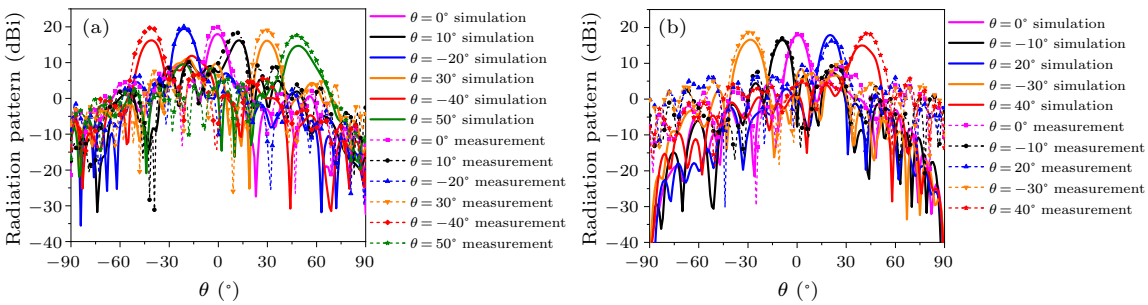


Fig. 18. Comparison of the co-polarized beam steering performance between the measurement and the simulation at 8.9 GHz: (a) *xoz* plane, (b) *yoz* plane.

Figure 18 shows comparison of the co-polarized beam steering performance between the measurement and the simulation at 8.9 GHz. Good agreement between them is observed as the radiation beam steers from 0° to 50°. The measured peak gains in *xoz* and *yoz* planes are 20.08 dBi and 18.68 dBi, with the aperture efficiencies of 24.95% and 18.07%, respectively. The measured SLL is better than −10 dB and the measured HPBW is less than 14° in the beam scanning range. Figure 19 shows the variation of the gain with the frequency for the broadside radiation. The measured 1 dB gain bandwidth covering 8.6–9 GHz with the fractional bandwidth of 4.55 % is slightly smaller than the simulated one of 8.6–9.17 GHz with the fractional bandwidth of 6.42%. The measured 3 dB gain bandwidth is 8.3–9.2 GHz with the fractional bandwidth

of 10.29%, which is slightly larger than the simulated one of 8.5–9.35 GHz with the fractional bandwidth of 9.52%. The slight discrepancy is attributed to the fabrication errors, substrate tolerance, and the experiment errors, etc.

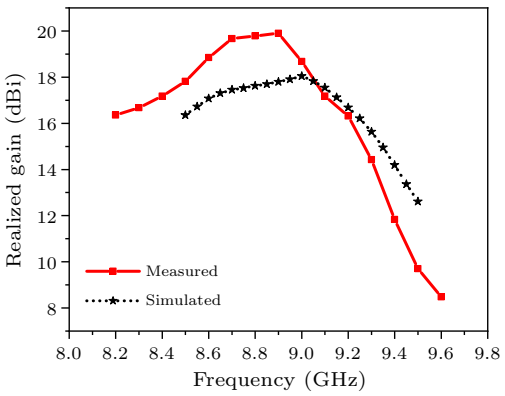


Fig. 19. Variation of the gain with the frequency for the co-polarized radiation.

The simulated and measured beam steering performance for the cross-polarized radiation is shown in Fig. 20, in good agreement. The measured peak gain and the aperture efficiency in *xoz* plane are 17.26 dBi and 13.3% and those in *yoz* plane are 16.62 dBi and 11.23% within the scanning range of ±60°. In the beam scanning range, the SLL better than −10 dB and the HPBW less than 17° are achieved. It can be seen from Fig. 21 that the measured 1 dB and 3 dB gain bandwidths cover 8.7–8.9 GHz and 8.5–9.1 GHz, respectively, slightly smaller than the simulated ones of 8.74–9.3 GHz and 8.55–9.5 GHz.

For the CP radiation, as shown in Fig. 15, the simulated beam scanning range for the gain drop ⩽ 3 dB covers 0° to 50°. In addition, Fig. 22 shows variation of the simulated LHCP gain with the frequency. The 1 dB and 3 dB gain bandwidths cover 8.91–9.41 GHz and 8.64–9.5 GHz, respectively.

Table 2 gives performance comparison between the proposed metasurface RRA design and the similarly reported designs. It can be found that the proposed reflectarray achieves the 2D beam steering and the polarization manipulations including linear co-polarized and cross-polarized radiations and circular cross-polarization radiation. Moreover, the wide beam scanning range for the gain drop no more than 3 dB is achieved, with the moderate 3 dB gain bandwidth and the aperture efficiency.

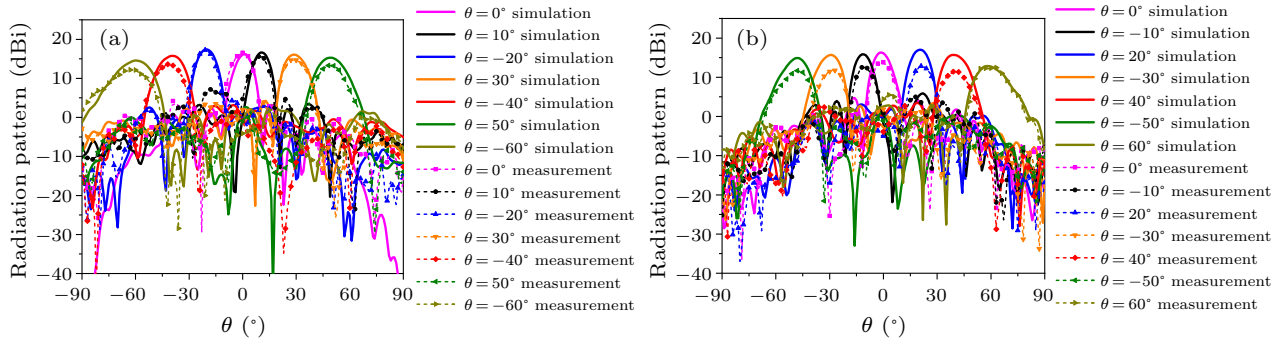


Fig. 20. Comparison of the cross-polarized beam steering performance between the measurement and the simulation at 8.9 GHz: (a) *xoz* plane, (b) *yoz* plane.

Table 2. Performance comparison between the proposed design and the reported designs.

References	Size (λ^2)	Polarization	Maximal scanning angle (°)	3 dB gain bandwidth (GHz)	Aperture efficiency (%)	Peak gain (dBi/dBic)
[19]	7.04 × 7.04 @12.6 GHz	Co-polarized (x)	*xoz*: 60 *yoz*: 45	12.05–13.5 (11.06%)	27.1	22.3
	8 × 8 @14.25 GHz	Co-polarized (y)	*xoz*: 45 *yoz*: 60	13.6–15.3 (11.9%)	22.2	22.5
[20]	7.6 × 7.6 @9.5 GHz	Co-polarized (LHCP)	*xoz*: 60 *yoz*: 45	9.07–9.8 (7.5%)	20	21.8
[21]	7.6 × 7.6 @15 GHz	Co-polarized (y)	*xoz*: 40 *yoz*: 50	–	25	21.6
[22]	8 × 8 @73.5 GHz	Cross-polarized (y)	30	71.5–76 (6.5%)	6.38	17.1
[23]	6.4 × 6.4 @10 GHz	Cross-polarized (x)	45	8.5–11.5 (30%)	17.1	18.5
This work	5.7 × 5.7 @8.9 GHz	Co-polarized (y/x)	*xoz*: 50 *yoz*: 40	8.3–9.2 (10.29%)	24.95	20.08
		Cross-polarized (x/y)	*xoz*: 60 *yoz*: 60	8.5–9.1 (6.28%)	13.03	17.26
		Cross-polarized (LHCP)	*xoz*: 50 *yoz*: 50	8.64–9.5 (9.48%)	11.96	16.98

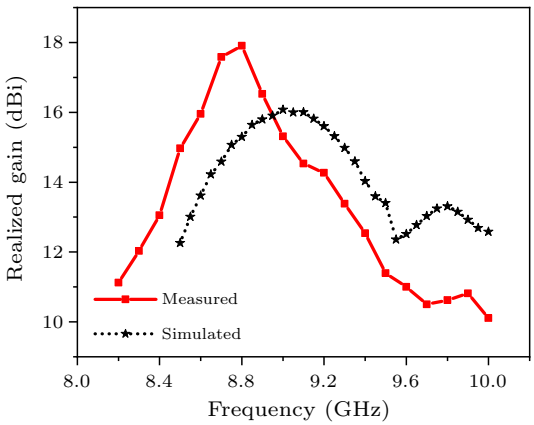


Fig. 21. Variation of the gain with the frequency for the cross-polarized radiation.

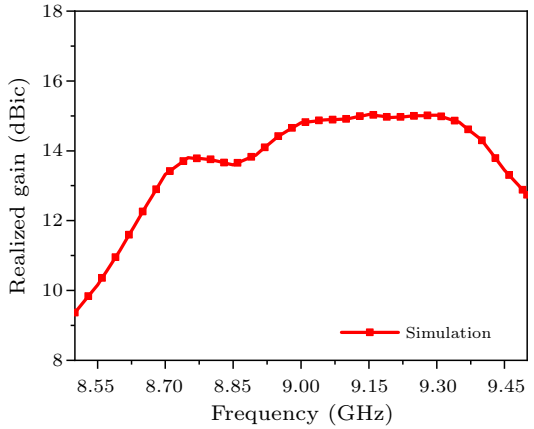


Fig. 22. Variation of the gain with the frequency for the CP radiation.

5. Conclusion and perspectives

In summary, a 1-bit electronically reconfigurable metasurface reflectarray with beam steering and polarization manipulation capabilities has been developed. A simple topology integrated with two PIN diodes is designed. By switching the PIN diodes between ON state and OFF state, the proposed unit cell operates four states, two of them exhibiting the cross-polarized responses and the others showing the co-polarized characteristics. Therefore, two groups of 1-bit unit cells are achieved for the cross-polarized and co-polarized radiations, respectively. Under the illumination by a linearly polarized wave, the designed metasurface RRA can achieve the 2D co-polarization and cross-polarization beam steering. When the RHCP wave is incident on the RRA, the LHCP beam scanning is realized. The 12×12 RRA prototype is fabricated. Measured results are given to demonstrate the wide beam scanning range of about $\pm 50^{\circ}$ and the good aperture efficiencies of about 25% for co-polarization radiation and about 13% for the cross-polarization radiation, meaning that the proposed metasurface RRA is a good candidate for wireless communication in the complex environment.

Acknowledgments

Project supported by the National Key Research and Development Program of China (Grant No. 2021YFA1401001) and the National Natural Science Foundation of China (Grant No. 62371355).

References

[1] Hum S V and Perruisseau-Carrier J 2014 *IEEE Trans. Antennas Propag.* **62** 183
[2] Nayeri P, Yang F and Elsherbeni A 2015 *IEEE Antennas Propag. Mag.* **57** 32
[3] Wang H L, Ma H F and Cui T J 2022 *Adv. Sci.* **9** 2204333
[4] Mirmozafari M, Zhang Z, Gao M, Zhao J, Honari M M, Booske J H and Behada N 2021 *Appl. Sci.* **11** 6890
[5] Yang X, Xu S H, Yang F, Li M K, Hou Y Q, Jiang S D and Liu L 2017 *IEEE Trans. Antennas Propag.* **65** 3959
[6] Bildik S, Dieter S, Fritzsch C, Menzel W and Jakoby R 2015 *IEEE Trans. Antennas Propag.* **63** 122
[7] Carrasco E and Perruisseau-Carrier J 2013 *IEEE Antennas Wireless Propag. Lett.* **12** 253
[8] Perruisseau-Carrier J 2010 *IEEE Trans. Antennas Propag.* **58** 1494
[9] Boccia L, Amendola G and Di Massa G 2010 *IEEE Trans. Antennas Propag.* **58** 585
[10] Kamoda H, Iwasaki T, Tsumochi J, Kuki T and Hashimoto O 2011 *IEEE Trans. Antennas Propag.* **59** 2524
[11] Han J Q, Li L, Liu G Y, Wu Z and Shi Y 2019 *IEEE Antennas Wireless Propag. Lett.* **18** 1268
[12] Rajagopalan H, Rahmat-Samii Y and Imbriale W A 2008 *IEEE Trans. Antennas Propag.* **56** 3689
[13] Guclu C, Perruisseau-Carrier J and Civi O 2012 *IEEE Trans. Antennas Propag.* **60** 5451
[14] Yang H H, Yang F, Xu S H, Mao Y L, Li M K, Cao X Y and Gao J 2016 *IEEE Trans. Antennas Propag.* **64** 2246
[15] Yang H H, Yang F, Cao X Y, Xu S H, Gao J, Chen X B, Li M K and Li T 2017 *IEEE Trans. Antennas Propag.* **65** 3024
[16] Pan X, Yang F, Xu S and Li M 2021 *IEEE Trans. Antennas Propag.* **69** 173
[17] Wang Z L, Ge Y H, Pu J X, Chen X X, Li G W, Wang Y F, Liu K T, Zhang H and Chen Z Z 2020 *IEEE Trans. Antennas Propag.* **68** 6806
[18] Luyen H, Booske J H and Behdad N 2020 *IEEE Trans. Antennas Propag.* **70** 4414
[19] Xu H J, Xu S H, Yang F and Li M K 2020 *IEEE Antennas Wireless Propag. Lett.* **19** 1896
[20] Wu F, Lu R, Wang J, Jiang Z H, Hong W and Luk K M 2021 *IEEE Trans. Antennas Propag.* **69** 5585
[21] Zhou S G, Zhao G, Xu H, Luo C W, Sun J Q, Chen G T and Jiao Y C 2021 *IEEE Antennas Wireless Propag. Lett.* **21** 566
[22] Liu C H, Ren Y L, Yang F, Xu S H and Li M K 2022 IEEE *16th European Conference on Antennas and Propagation (EuCAP)*, March 27–April 01, 2022, Madrid, Spain, pp. 1–3
[23] Luyen H, Zhang Z, Booske J H and Behdad N 2022 *IEEE Trans. Antennas Propag.* **70** 4414
[24] Shi Y, Chu P P and Meng Z K 2023 *J. Phys. D: Appl. Phys.* **56** 095102
[25] Shi Y, Chu P P and Meng Z K 2022 *Wave Random Complex Media*
[26] Yang H H, Yang F, Xu S H, Li M K, Cao X Y, Gao J and Zheng Y J 2016 *IEEE Antennas Wireless Propag. Lett.* **16** 302
[27] Yu A, Yang F, Elsherbeni A Z, Huang J and Rahmat-Samii Y 2010 *Microw. Opt. Technol. Lett.* **52** 364